Aggregation control in natural brush-printed conjugated polymer films and implications for enhancing charge transport

Gang Wang[a,b,c], Wei Huang[a,b,c], Nicholas D. Eastham[a,b,c], Simone Fabiano[a,d,e], Eric F. Manley[a,f], Li Zeng[g], Binghao Wang[a,b,c], Xinan Zhang[a,b,c], Zhihua Chen[d], Ran Li[b,c,h], Robert P. H. Chang[b,c,h], Lin X. Chen[a,b,c,f], Michael J. Bedzyk[b,c,g,h], Ferdinand S. Melkonyan[a,b,c], Antonio Facchetti[a,b,c,d,1], and Tobin J. Marks[a,b,c,h,1]

[a]Department of Chemistry, Northwestern University, Evanston, IL 60208; [b]The Materials Research Center, Northwestern University, Evanston, IL 60208; [c]The Argonne–Northwestern Solar Energy Research Center, Northwestern University, Evanston, IL 60208; [d]Flexterra, Inc., Skokie, IL 60077; [e]Laboratory of Organic Electronics, Department of Science and Technology, Linköping University, Norrköping SE-60174, Sweden; [f]Chemical Sciences and Engineering Division, Argonne National Laboratory, Lemont, IL 60439; [g]Graduate Program in Applied Physics, Materials Research Center, Northwestern University, Evanston, IL 60208; and [h]Department of Materials Science and Engineering, Northwestern University, Evanston, IL 60208

Contributed by Tobin J. Marks, October 6, 2017 (sent for review April 17, 2017; reviewed by Zhenan Bao and Natalie Stingelin)

Shear-printing is a promising processing technique in organic electronics for microstructure/charge transport modification and large-area film fabrication. Nevertheless, the mechanism by which shear-printing can enhance charge transport is not well-understood. In this study, a printing method using natural brushes is adopted as an informative tool to realize direct aggregation control of conjugated polymers and to investigate the interplay between printing parameters, macromolecule backbone alignment and aggregation, and charge transport anisotropy in a conjugated polymer series differing in architecture and electronic structure. This series includes (*i*) semicrystalline hole-transporting P3HT, (*ii*) semicrystalline electron-transporting N2200, (*iii*) low-crystallinity hole-transporting PBDTT-FTTE, and (*iv*) low-crystallinity conducting PEDOT:PSS. The (semi-)conducting films are characterized by a battery of morphology and microstructure analysis techniques and by charge transport measurements. We report that remarkably enhanced mobilities/conductivities, as high as 5.7×/3.9×, are achieved by controlled growth of nanofibril aggregates and by backbone alignment, with the adjusted R^2 (R^2_{adj}) correlation between aggregation and charge transport as high as 95%. However, while shear-induced aggregation is important for enhancing charge transport, backbone alignment alone does not guarantee charge transport anisotropy. The correlations between efficient charge transport and aggregation are clearly shown, while mobility and degree of orientation are not always well-correlated. These observations provide insights into macroscopic charge transport mechanisms in conjugated polymers and suggest guidelines for optimization.

natural brush-printing | shear effects | polymer alignment | polymer aggregation | polymer charge transport

The key attribute of fabrication processes for next-generation low-cost consumer electronic products composed of unconventional optoelectronic devices, such as organic photovoltaic (OPV) cells, organic LEDs, and organic field effect transistors (OFETs), will be economical solution deposition methodologies (1–4). However, to achieve these ends, it is essential that charge transport in the organic (semi-)conducting layer(s) of these devices meet rigorous performance and reliability standards for mass production (5–7). Science-based film processing techniques capable of increasing charge carrier mobility and electrical uniformity by manipulating/aligning the film microstructure typically rely on mechanical stretching, high-temperature rubbing, or shear-printing (8–10). Among these methodologies, shear-printing has been of primary interest because of its applicability to large-area film fabrication, microstructure control, and enhancement of charge transport characteristics. Shear effects have enabled long-range backbone orientation/alignment in conjugated polymers, thereby increasing charge transport metrics (5, 11, 12) as well as charge transport anisotropy (13, 14). Previous shear-printing studies have mainly explored the relationship between carrier mobility (μ) enhancement, charge transport anisotropy, and polymer backbone alignment, typically using the optical dichroic ratio (*DR*) to assess the degree of backbone alignment (9, 15, 16). For example, by controlling the ink flow directionality by bar-coating techniques, shear-aligned thin films of a naphthalediimide polymer exhibit highly oriented chains (*DR* = 4.8), substantial transport anisotropy (~20.1), and increased electron mobility (4.1 $cm^2 V^{-1} s^{-1}$) in the macromolecule alignment direction (9).

Curiously, however, a number of shear-aligned conjugated polymers are reported to exhibit negligible sensitivity of mobility/conductivity to *DR* (2, 17). For example, silicon blade-shearing of poly(diketopyrrolopyrrole-terthiophene) enhances the mobility from 0.35 to 0.80 $cm^2 V^{-1} s^{-1}$ with negligible transport anisotropy, yet a large *DR* = 7 is measured by polarized optical spectroscopy (17). Similarly, shear deposition of highly conductive poly(3,4-ethylenedioxythiophene):poly(styrenesulfonate) (**PEDOT:PSS**) films yields a record high conductivity, 4,600 vs. 860 S cm^{-1} for

Significance

Shear-printing of electroactive polymers using natural brushes is a promising film deposition technique for printed electronics capable of microstructure control and electrical properties enhancement over large areas. Nevertheless, the interplay between film printing parameters, microstructure development, and charge transport is not well-understood. We report that natural brush-printing greatly enhances charge transport by as much as 5.7× through control of polymer nanofibril aggregate growth and backbone alignment, attributable to the oriented squamae of the natural hair. However, while brush shear-induced aggregation enhances charge transport, we show that backbone alignment alone does not guarantee charge transport anisotropy. These results provide additional understanding of shear-induced enhanced charge transport and set processing guidelines for high-performance printed organic circuitry.

Author contributions: G.W., A.F., and T.J.M. designed research; G.W., W.H., N.D.E., S.F., E.F.M., L.Z., B.W., X.Z., Z.C., and R.L. performed research; G.W., M.J.B., F.S.M., A.F., and T.J.M. analyzed data; and G.W., W.H., S.F., R.P.H.C., L.X.C., M.J.B., F.S.M., A.F., and T.J.M. wrote the paper.

Reviewers: Z.B., Stanford University; and N.S., Georgia Institute of Technology.

The authors declare no conflict of interest.

[1]To whom correspondence may be addressed. Email: a-facchetti@northwestern.edu or t-marks@northwestern.edu.

This article contains supporting information online at www.pnas.org/lookup/suppl/doi:10.1073/pnas.1713634114/-/DCSupplemental.

the spin-coated films, with negligible transport anisotropy and $DR = 1.6$ (2). Thus, the interplay between shear conditions, thin-film microstructure evolution, and charge transport is far from clear, and a systematic investigation of a series of conjugated polymers differing in structure and electronic properties would be highly desirable.

Various techniques have been developed to induce polymer aggregation (defined as short-range ordered assemblies) and enhance charge transport, including poor solvent-related additions (18), UV irradiation (19, 20), and solution aging (21). However, such aggregation processes typically involve solutions, which may be difficult to control and have restricted process windows that are incompatible with manufacture. Shear-printing with physically etched micro-/nanostructured blades is a promising approach to enhance conjugated polymer alignment and crystallinity, hence charge transport (3, 5, 22). However, the fabrication of these artificial shear features relies on complicated, expensive photolithography and etching. An alternative methodologically simpler approach, brush-printing, a subset of shear-printing (23–25), enables the effective application of shear stress throughout a polymer solution, thereby promoting the extension, alignment, and aggregation of the macromolecular chains. Moreover, bio-derived brush-printing using natural hair offers a unique capacity to control liquid transfer, leading to uniform film formation (26, 27) (Fig. 1*A*). The oriented squamae along the natural hair axis should enhance shearing effects, leading to increased polymer aggregation and backbone alignment, in a manner roughly analogous to the physically etched micro-/nanostructured features noted above (3, 5).

Here, shear-printing using natural hairs, natural brush-printing, is utilized as an effective tool to directly control polymer aggregation and to systematically investigate charge transport in a series of model conjugated polymers differing in crystallinity, electronic structure, and charge transport characteristics. This group includes the semicrystalline hole-transporting semiconductor poly(3-hexylthiophene-2,5-diyl) (**P3HT**) (28), the semicrystalline electron-transporting semiconductor poly{[N,N′-bis(2-octyldodecyl)-naphthalene-1,4,5,8-bis(dicarboximide)-2,6-diyl]-alt-5,5′-(2,2′-bithiophene)} (**N2200**) (9), the low-crystallinity hole-transporting semiconductor poly[4,8-bis(5-(2-ethylhexyl)thiophen-2-yl)benzo-[1,2-b;4,5-b′]dithiophene-2,6-diyl-alt-(4-(2-ethylhexyl)-3-fluorothieno[3,4-b]thiophene-)-2-carboxylate-2–6-diyl)] (**PBDTT-FTTE**) (29–31), and the low-crystallinity conducting polymer **PEDOT:PSS** (32) (Fig. 1 *B*–*E*). The microstructures of the directionally brush-printed films are investigated in detail by polarized optical spectroscopy, atomic force microscope (AFM), polarized optical microscopy (POM), and grazing incidence wide-angle X-ray scattering (GIWAXS). Charge transport is investigated in OFETs and also by four-point probe conductivity. Importantly, it will be seen that the adjusted R^2 (R^2_{adj}) correlation between aggregation and charge transport is as high as 95%. Shear can promote backbone alignment, thus facilitating aggregation and enhanced charge transport mobility, but cannot necessarily induce charge transport anisotropy for reasons that will be clarified. These results provide additional understanding of shear-induced enhanced charge transport and set processing guidelines for the next generation high-performance printed organic circuitry.

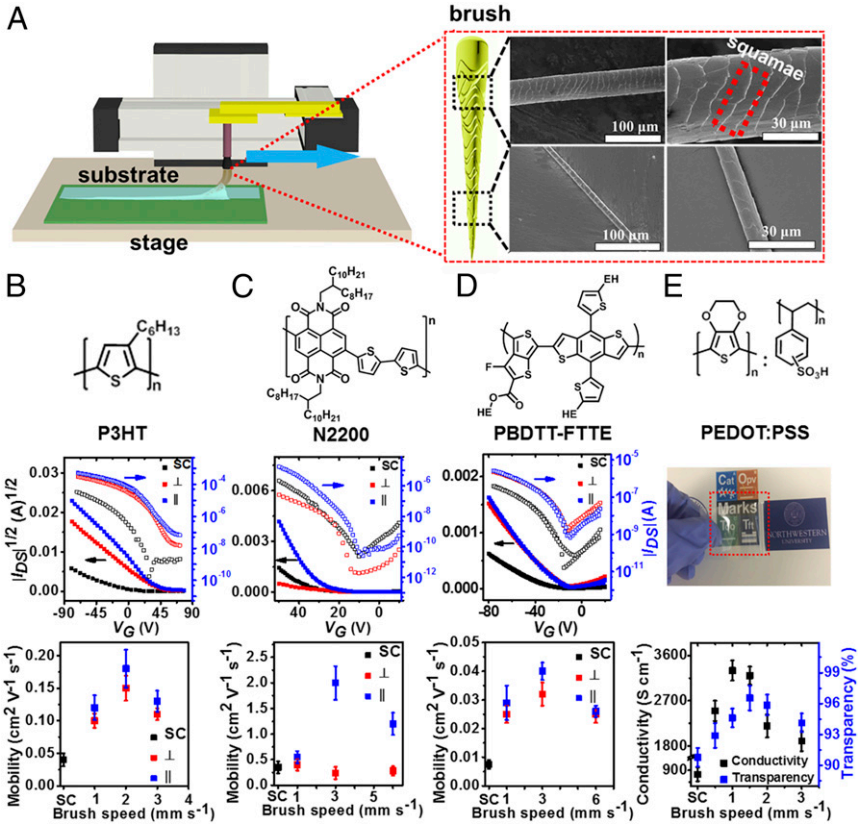

Fig. 1. Charge transport characteristics of conjugated polymers deposited by brush-printing. (*A*) Schematic of brush-printing setup including SEM images of the brush natural hair with squamae structures. For (*B*) **P3HT**, (*C*) **N2200**, and (*D*) **PBDTT-FTTE**, chemical structures, typical OFET transfer plots, and corresponding saturation mobilities are shown. (*E*) For **PEDOT:PSS**, chemical structure, optical image of a bent 2.5 × 5.0-cm **PEDOT:PSS** film fabricated by brush-printing on a polyethylene terephthalate substrate (red border added to guide the eye), and electrical conductivity and optical transparency vs. brush speed are shown. SC, spin-coated film.

Results and Discussion

Brush-Printing and Charge Transport. The brush-printing setup is shown in Fig. 1*A*, with additional details presented in *Methods* and *SI Appendix*. To quantify charge transport properties and how they are influenced by the polymer deposition methodology and parameters, OFETs with top-gate, bottom-contact architectures were fabricated with **P3HT**, **N2200**, and **PBDTT-FTTE**, whereas conducting lines were fabricated for **PEDOT:PSS**. Transport metrics are summarized in Tables 1 and 2. The transport properties of brush-printed **P3HT** films in OFETs were first investigated, printing at a speed (ν) of 2.0 mm s^{-1}, in both directions parallel (||) and perpendicular ($\perp$) to the source to drain electric field vs. those fabricated by spin-coating (SC). Typical OFET transfer characteristics (Fig. 1*B*) show clear current modulation and saturation. The corresponding μ values were measured in saturation and calculated using standard MOSFET models (1). Spin-coated **P3HT** films exhibit a charge-carrier mobility (μ_{sc}) of 0.04 cm^2 V^{-1} s^{-1}, comparable with that reported in other studies (19, 22, 33). For the brush-printed films, a 4.5× increase in carrier mobility is achieved in both the parallel and perpendicular directions compared with spin-coated samples, resulting in $\mu_{||}/\mu_{\perp}$ = 0.18/0.15 cm^2 V^{-1} s^{-1}. Thus, brush-printing enhances the carrier mobility, but the charge transport anisotropy ($\mu_{||}/\mu_{\perp}$) is only 1.2. The impact of the brush speed (ν = 1.0, 2.0, and 3.0 mm s^{-1}) on the **P3HT** OFET performance was also evaluated, and $\mu_{||}$ increases from 0.12 to 0.18 cm^2 V^{-1} s^{-1} as ν increases from 1.0 to 2.0 mm s^{-1}, while $\mu_{||}/\mu_{\perp}$ is unchanged. Additional increase in ν to 3.0 mm s^{-1} result in decline to 0.13 cm^2 V^{-1} s^{-1}. Typical transfer characteristics of **N2200**-based OFETs are shown in Fig. 1*C*. In contrast to **P3HT**, **N2200**-based OFETs fabricated with brush-printed films at optimal deposition speeds exhibit significantly enhanced mobility and charge transport anisotropy. Compared with spin-coated devices, where μ_{sc} = 0.35 cm^2 V^{-1} s^{-1}, $\mu_{||}$ for the devices brush-printed at 1 mm s^{-1} is far larger, and the mobility anisotropy of $\mu_{||}/\mu_{\perp}$ = 0.55/0.40 cm^2 V^{-1} s^{-1}. Moreover, as ν increases to 3 mm s^{-1}, $\mu_{||}/\mu_{\perp}$ = 2.0/0.24 cm^2 V^{-1} s^{-1} for a maximum mobility increase of 5.7× and an anisotropy of ∼8.3. For **PBDTT-FTTE**–based OFETs (Fig. 1*D*), the brush-printed films at optimal deposition speeds afford increased mobility but with minimal charge transport anisotropy. Interestingly, compared with spin-coated devices, where μ_{sc} = 0.0075 cm^2 V^{-1} s^{-1}, the mobility anisotropy is only 1.16 ($\mu_{||}/\mu_{\perp}$ = 0.029/0.025 cm^2 V^{-1} s^{-1}) for devices brush-printed at 1 mm s^{-1}. As ν increases to 3 mm s^{-1}, $\mu_{||}/\mu_{\perp}$ = 0.04/0.032 cm^2 V^{-1} s^{-1} for a mobility anisotropy of ∼1.25. Finally, for a very large ν = 6 mm s^{-1}, the mobility anisotropy is 1.04, and $\mu_{||}/\mu_{\perp}$ = 0.026/0.025 cm^2 V^{-1} s^{-1}.

Table 1. Performance metrics of semiconductors (OFETs) fabricated by spin-coating or brush-printing

OFET metrics*	μ (cm^2 V^{-1} s^{-1})	V_{th} (V)	I_{on}/I_{off}
P3HT (SC)	0.04 ± 0.01	27 ± 3	(2 ± 0.3) × 10^5
P3HT (||)†	0.18 ± 0.03	35 ± 5	(2 ± 0.3) × 10^4
P3HT ($\perp$)†	0.15 ± 0.02	39 ± 6	(1 ± 0.3) × 10^4
N2200 (SC)	0.35 ± 0.12	25 ± 5	(2 ± 0.3) × 10^5
N2200 (||)‡	2.0 ± 0.33	22 ± 4	(4 ± 0.4) × 10^5
N2200 ($\perp$)‡	0.24 ± 0.12	−(1.5 ± 1)	(1 ± 0.2) × 10^6
PBDTT-FTTE (SC)	(7.5 ± 1.5) × 10^{-3}	−(7 ± 3)	(6 ± 0.3) × 10^3
PBDTT-FTTE (||)§	0.04 ± 0.004	−(11 ± 3)	(5 ± 0.4) × 10^3
PBDTT-FTTE ($\perp$)§	0.032 ± 0.004	−(12 ± 3)	(3 ± 0.4) × 10^3

SC, spin-coating.
*Data are the average of ≥10 devices.
†ν = 2 mm s^{-1}.
‡ν = 3 mm s^{-1}.
§ν = 3 mm s^{-1}.

Table 2. Performance metrics for conductors fabricated by spin-coating or brush-printing

Conductor metrics*	Conductivity (S cm^{-1})	Transparency (%)
PEDOT:PSS (SC)	850 ± 87	90.8 ± 0.9
PEDOT:PSS (||)†	3,198 ± 200	96.5 ± 0.9
PEDOT:PSS ($\perp$)†	3,160 ± 200	96.30 ± 1.1

SC, spin-coating.
*Data are the average of ≥10 devices.
†ν = 1.5 mm s^{-1}.

The effect of the brush-printing process vs. spin-coating and brush speed effects on the four-point probe electrical conductivity and optical transparency of **PEDOT:PSS** films are shown in Fig. 1*E*, Tables 1 and 2, and *SI Appendix*, Table S1. These data indicate that, while the brush-printed films are more conductive and transparent than the spin-coated ones, negligible anisotropy in the electrical and optical characteristics is observed. Thus, the conductivity first increases from 2,500 S cm^{-1} (ν = 0.5 mm s^{-1}) to 3,300 S cm^{-1} (ν = 1.0 mm s^{-1}) and then falls to 1,900 S cm^{-1} for ν = 3.0 mm s^{-1} vs. only 850 S cm^{-1} for the spin-coated films. Concomitantly, the film optical transmittance increases from 92.9% (0.5 mm s^{-1}) to 94.6% (1.0 mm s^{-1}). Notably, ν = 1.5 mm s^{-1} is found to achieve the optimal balance between conductivity (3,198 S cm^{-1}) and transparency (96.6%) and is among the highest reported performance for **PEDOT:PSS** films (2). The high conductivity and transparency of these brush-printed **PEDOT:PSS** films yield excellent transparent conducting anodes for devices, such as OPVs (*SI Appendix*, Fig. S1 and Table S2).

Film Morphological Analysis. The long-range domain order and details of film morphology in these brush-printed polymers were first investigated by POM and AFM, with metrics summarized in Table 3. For brushed-printed **P3HT** films, POM shows nearly complete extinction and reemergence of brightness on rotation of the channel long axis from 0° to 45° (Fig. 2*A* and *SI Appendix*, Fig. S2), suggesting long-range order over the dimensions of the brush-printing direction. From AFM phase mode images (Fig. 2*A*), the surface topology is composed primarily of oriented **P3HT** fibers. The density and dimensions of the nanofibers increase dramatically on brush-printing (*SI Appendix*, Fig. S3). Statistical analysis of the topology (images in *SI Appendix*, Fig. S3) using the FiberAPP software (34) indicates that the average fiber dimensions increase from 600 × 45 to 900 × 60 nm from spin-coating to brush-printing (ν = 2 mm s^{-1}), respectively, the latter clearly exhibiting nanofibril growth. The corresponding optical absorption spectra (*SI Appendix*, Fig. S4) indicate an increase in the **P3HT** 0–0 and 0–1 vibronic features at 620 and 564 nm, respectively, showing enhanced **P3HT** interchain π–π interactions and aggregation (35–37). The degree of **P3HT** aggregation in the film [i.e., the aggregation fraction (*AF*)] as a function of processing methodology was quantified from Franck–Condon fits of the optical absorption spectra, and data are shown in Fig. 2*B* (28, 38, 39). Compared with the spin-coated **P3HT** films with *AF* = 22%, brush-printing enhances the *AF* dramatically as the brushing rate increases from 1 mm s^{-1} (*AF* = 26%) to 2 mm s^{-1} (*AF* = 36%) and then declines as the brushing rate increases to 3 mm s^{-1} (*AF* = 28%). The degree of **P3HT** film backbone alignment was next quantified from the optical *DR* measured using polarized ultraviolet-visible absorption spectroscopy (UV-Vis). From Fig. 2*B* and *SI Appendix*, Fig. S5, while the *DR* of the spin-coated **P3HT** films is 1.0, brush-printing increases the *DR* first from 1.8 to 3.0 and then, to a maximum of 3.5 as the brush-printing speed increases from 0.5 to 2 to 2.5 mm s^{-1}, respectively. Beyond a speed of 3 mm s^{-1}, the *DR* falls to 2.6. For **N2200** films, POM analysis and AFM images (Fig. 2*C* and *SI Appendix*, Figs. S6 and S7) indicate long-range order and the

Table 3. Statistical analysis of nanofibril dimensions using Fiber APP software and *DR*, *AF*, and *RA* of various conjugated polymer systems via spin-coating and brush-printing

Microstructure metrics	Nanofiber dimensions (nm^2)	*DR*	*AF* (%)	*RA*
P3HT (SC)*	600 × 45	1.0	23 ± 2	1.0
P3HT (BP)†	900 × 60	3.0 ± 0.2	36 ± 3	1.5
N2200 (SC)*	900 × 55	1.0	48 ± 2	1.0
N2200 (BP)‡	1,400 × 125	4.6 ± 0.3	63 ± 2	1.6
PBDTT-FTTE (SC)*	50 × 20	1.0	—	1.2
PBDTT-FTTE (BP)§	100 × 20	2.2 ± 0.2	—	1.32
PEDOT:PSS (SC)*	—	1.0	—	—
PEDOT:PSS (BP)¶	250 × 50	1.6 ± 0.1	—	2.3

BP, brush-printing; SC, spin-coating.
*Calculated from the spin-coated samples.
†ν = 2 mm s^{-1}.
‡ν = 3 mm s^{-1}.
§ν = 3 mm s^{-1}.
¶ν = 1.5 mm s^{-1}.

formation of oriented nanofibers along the brush-printing direction. From AFM statistical analysis, the fiber dimensions increase from 900 × 55 nm (spin-coating) to 1,600 × 125 nm for brush-printing (ν = 3 mm s^{-1}). The principle absorption band at ~700 nm with a shoulder at ~780 nm is attributed to the formation of aggregated species, while the band at ~600 nm is associated with nonaggregated macromolecules (39). The enhanced intensity of the red-shifted optical absorption band on brush-printing suggests increased aggregation, and data analysis (Fig. 2*D* and *SI Appendix*, Fig. S8) indicates that brush-printing substantially increases the *AF*, with *AF* = 52, 63, and 57% for ν = 1, 3, and 6 mm s^{-1}, respectively. Similarly, using *DR* to quantify **N2200** backbone alignment (*SI Appendix*, Fig. S9) reveals that brush-printing enhances *DR* to a maximum of 4.6 for ν = 3 mm s^{-1}.

For **PBDTT-FTTE** films, the POM analysis and AFM images (Fig. 2*E* and *SI Appendix*, Figs. S10 and S11) indicate long-range order and the formation of well-defined nanofibers. From AFM statistical analysis, the fiber dimensions increases from 50 × 20 nm (spin-coating) to 100 × 20 nm for the brush-printed samples (ν = 3 mm s^{-1}). From UV-Vis spectra of the **PBDTT-FTTE** films (*SI Appendix*, Fig. S12), there is an absorbance maximum at λ_{max} ~ 700 nm (A_{0-0}), with a secondary maximum at ~650 nm (A_{0-1}), and the (A_{0-0}/A_{0-1}) ratio can be correlated with the extent of macromolecular aggregation, with larger values indicating greater aggregation (40). Note also that **PBDTT-FTTE** in spin-coated films with A_{0-0}/A_{0-1} = 1.20 is less aggregated than the brush-printed films (ν = 3 mm s^{-1}), with a maximum A_{0-0}/A_{0-1} = 1.32. Fig. 2*F* and Table 3 summarize the **PBDTT-FTTE** aggregation data. Similarly, quantitative *DR* analysis of **PBDTT-FTTE** backbone alignment (*SI Appendix*, Fig. S13) indicates that brush-printing enhances *DR* to a maximum of 2.3 at ν = 6 mm s^{-1}. Interestingly, negligible long-range orientation of **PEDOT:PSS** polymer domains can be detected in the POM images (Fig. 2*G* and *SI Appendix*, Fig. S14) of brush-printed samples at all speeds. However, the corresponding AFM images (Fig. 2*H*) indicate that brush-printing promotes formation of well-defined nanofibers vs. the 30-nm-diameter small spherical particles produced by spin-coating (*SI Appendix*, Fig. S15). The formation of nanofibrils is attributed to the interchain **PEDOT:PSS** aggregation in the brush-printed samples (2, 32, 41). AFM statistical analysis reveals that the average nanofiber length first increases from 190 to 290 nm as ν increases from 0.5 to 1 mm s^{-1} and then decreases (250 → 180 → 125 nm) for increasing ν values (1.5 → 2 → 3 mm s^{-1}, respectively). For both **P3HT** and **N2200**, the nanofiber lengths obtained from spin-coating and brush-printing correlate well with the respective *AF*s, and similar phenomena have been reported for typical conjugated polymer nanofiber aggregations in **P3HT** and **N2200** (9, 21). In the present study, the ratio of the nanofiber lengths was determined as relative aggregation (*RA*), with the smallest nanofiber dimension defined as 1.0. Thus, for **PEDOT:PSS**, the nanofiber dimensions calculated from the AFM images (*SI Appendix*, Fig. S15) were used to quantify the aggregation. It is found that there is negligible nanofiber aggregation in the spin-coated films. The lowest level of *RA* (smallest fiber lengths) for brush-printed **PEDOT:PSS** films is achieved when ν = 6 mm s^{-1}. If *RA* for these samples is normalized to 1.0, it increases from 1.5 to 2.3 and then decreases to 1.5 as ν is increased from 0.5 to 1 mm s^{-1}, respectively (Fig. 2*H*). In comparison, *DR* for these same brush-

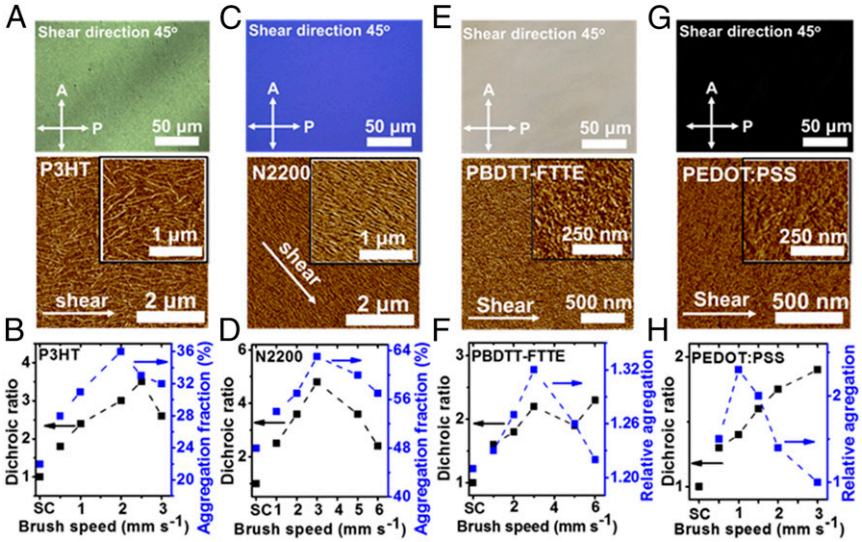

Fig. 2. Conjugated polymer film morphology and backbone alignment analysis. (*A*, *C*, *E*, and *G*) Representative POM images (*Upper*; arrows denote directions of crossed polarizers) and tapping mode AFM images (*Lower*; *Insets* show magnification) of (*A*) **P3HT** (ν = 2 mm s^{-1}), (*C*) **N2200** (ν = 3 mm s^{-1}), (*E*) **PBDTT-FTTE** (ν = 3 mm s^{-1}), and (*G*) **PEDOT:PSS** (ν = 1.5 mm s^{-1}). The *DR* and *AF* (or *RA*) of polymer films via spin-coating and brush-printing for the indicated brush speeds are shown for (*B*) **P3HT**, (*D*) **N2200**, (*F*) **PBDTT-FTTE**, and (*H*) **PEDOT:PSS**.

printed **PEDOT:PSS** films (*SI Appendix*, Fig. S16) is >1.0 and increases from 1.3 to 1.9 when ν increases from 0.5 to 3 mm s^{-1}, respectively. Note that these *DR*s are even larger than those reported for solution-sheared **PEDOT:PSS** films, having maximum conductivity (2). In other work, it was shown that increased poly(3,4-ethylenedioxythiophene) (**PEDOT**) chain ordering increases conductivity (2, 32, 41), in agreement with these brush-printing results.

GIWAXS Analysis. The microstructures of **P3HT**, **N2200**, **PBDTT-FTTE**, and **PEDOT:PSS** films were characterized by GIWAXS at beamline 8-ID-E of the Advanced Photon Source. The diffraction patterns shown in Fig. 3 *A*, *C*, *E*, and *G* were recorded on a planar area detector, and line cut profiles are shown in *SI Appendix*, Figs. S17–S20. The GIWAXS-derived structural parameters are summarized in *SI Appendix*, Table S3 (16, 18). The GIWAXS **P3HT** film profiles (Fig. 3*A*) exhibit several (h 0 0) reflections along the out-of-plane (q_z) direction, corresponding to **P3HT** lamellar stacking normal to the substrate surface (42). The crystal orientation was next quantified by the Hermans' orientation factor, f_H (33). For the **P3HT** (1 0 0) reflection, f_H ranges from −0.5 to 1.0, where 1.0 corresponds to perfectly oriented crystal planes perpendicular to the substrate ("edge-on"), −0.5 denotes a lattice plane strictly oriented parallel ("face-on"), and randomly oriented structures have a value of 0. The f_H of the brush-printed samples is as high as 0.64, indicating a microstructure with primarily edge-on orientation. It has been reported that the characteristic π–π stacking peak should exhibit maximum intensity when the X-ray incident beam is aligned along the polymer backbone (17, 28). Thus, the distinct intensity of the (0 1 0) reflection of the brush-printed films between the || and ⊥ directions provides additional support that the polymer backbones are well-aligned and oriented perpendicular to the brush-printing direction. Thus, the combined GIWAXS, polarized UV-Vis, and POM data indicated that the **P3HT** polymer chains are edge-on distributed and π–π stacked along the brush-printed direction to form aggregated nanofibrils (Fig. 3*B*).

GIWAXS measurements on brush-printed **N2200** films (Fig. 3*C*) indicate preferential face-on polymer crystallite orientation. Additionally, the Hermans' orientation parameter is ∼−0.47 for the brush-printed films, indicating a highly face-on oriented crystalline stacking. The (0 0 1) in-plane stacking peak is located at 0.46 $Å^{-1}$, corresponding to a (0 0 1) *d* spacing of ∼3.50 Å and indicating more dense stacking than in the spin-coated films. Furthermore, the relative in-plane backbone scattering intensity is greater for X-ray incidence perpendicular to the brush-printing direction, consistent with polymer backbone alignment parallel to the brush-printing direction (9). Thus, combining this GIWAXS analysis with the polarized UV-Vis reveals that the **N2200** stacking is distributed face-on, with the backbone aligned parallel to the brush-printing direction (43, 44) (Fig. 3*D*).

For **PBDTT-FTTE** samples, the GIWAXS data (Fig. 3*E*) indicate preferential face-on orientation and relatively weaker intensities compared with brush-printed **P3HT** and **N2200** films (40). Additionally, the Hermans' orientation parameter of ∼−0.29 for the brush-printed films indicates a highly face-on oriented crystalline stacking. Owing to the low crystallinity, no backbone alignment information can be obtained from the GIWAXS. Combining the GIWAXS and polarized UV-Vis data indicates that intermolecular **PBDTT-FTTE** stacking is face-on distributed, with the backbone aligned parallel to the brush-printing direction (Fig. 3*F*). Finally, the **PEDOT:PSS** film GIWAXS reflections at 0.60 and 1.85 $Å^{-1}$ (Fig. 3*G* and *SI Appendix*, Fig. S15) in the out-of-plane direction represent the (1 0 0) lamellar and (0 1 0) π–π stacking, respectively, and there is

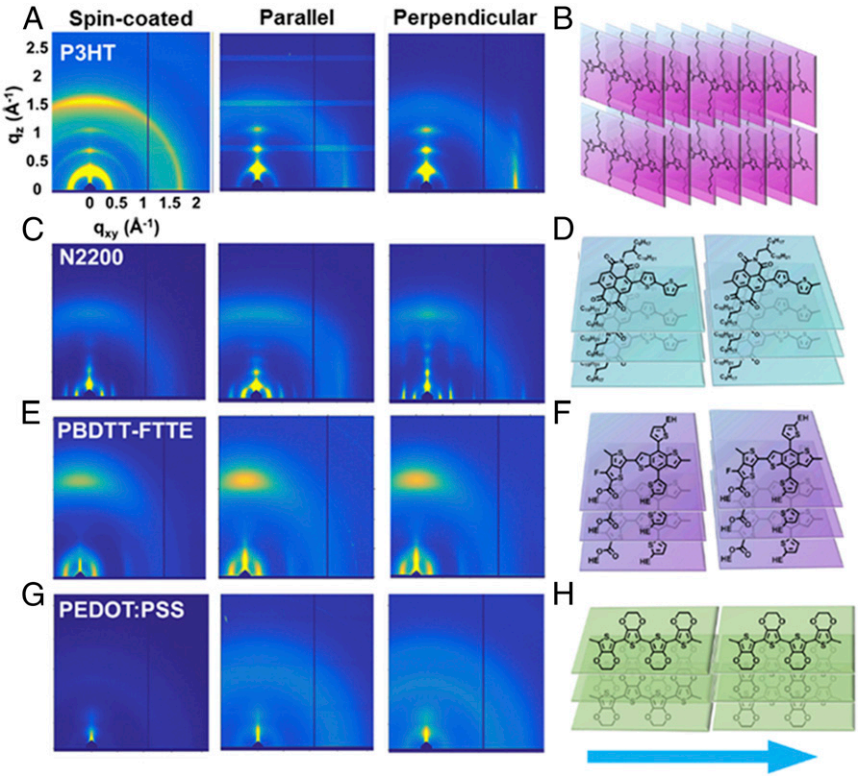

Fig. 3. GIWAXS analysis of the indicated conjugated polymer films deposited by brush-printing. GIWAXS patterns of (*A*) **P3HT**, (*C*) **N2200**, (*E*) **PBDTT-FTTE**, and (*G*) **PEDOT:PSS**. *B*, *D*, *F*, and *H* illustrate the molecular chain stacking of the brush-printed films, with the arrow indicating the brush-printing direction. The axis labeled in *A*, *Left* applies to all images.

a low-crystallinity poly(styrenesulfonate) reflection at 1.23 $Å^{-1}$ (32). The stronger reflection brush-printed film intensities indicate enhanced crystallinity (45). The films after brush-printing show stronger (1 0 0) reflections along the q_z axis vs. the q_{xy} axis, implying that **PEDOT** has preferred face-on packing (46). The combined GIWAXS and polarized UV-Vis indicate that **PEDOT:PSS** stacking is preferential face-on distributed, with the backbone aligned parallel to the brush-printing direction (Fig. 3*H*).

The Brush-Printing Process. At this point, it is important to clarify how brush-printing affects π-electron polymer film morphology as a general guideline for fabricating high-mobility conjugated polymer films. Utilizing **N2200** as a model, it can be seen that uniform films with increased nanofiber length (1.4×), backbone alignment (1.9×), enhanced *AF* (1.3×), and higher carrier mobility (1.5×) are obtained via brush-printing vs. a control deposited with a smooth artificial brush (Fig. 4*B* and *SI Appendix*, Table S4). These experimental results reveal that the natural brush squamae structure is effective in achieving substantial levels of polymer chain alignment and intermolecular aggregation. Similar to physically etched micro-/nanostructured features for shear-printing (3, 5, 22), the oriented natural squamae induced enhanced polymer chain alignment and controllable liquid transfer, resulting in unique microstructure control and mobility enhancement. The principle effects are proposed to be (*i*) polymer chain extension owing to the extensional flow during the liquid transfer process and (*ii*) shear effects during film formation process. We now discuss these effects.

Owing to the lower entropic barrier to forming ordered structures, shear-induced chain extension and alignment have long been known to enhance polymer aggregation and crystallization (47, 48). Among various flow modes, extensional flow has proven to be an effective strategy for promoting crystallization by stretching the polymer chains (49, 50). Extensional flow in continuous contraction channels is effective in inducing fibril structure formation with enhanced crystallinity (51, 52). During the brush-printing process, the contraction distribution toward the bottom of the bristles is maintained (26, 27). As we propose in Fig. 4*A*, *Left*, for the liquid transfer process, owing to the special contraction geometry of the liquid transfer channels in the natural brush-printing, the extensional flow is expected to promote polymer chain extension and nanofibril microstructure formation (52). For the film formation process shown in Fig. 4*A*, *Right*, shear effects are expected to further promote polymer chain orientation and nanofibril aggregation. In the case of a Newtonian polymer solution, the shear stress causes the organization of polymer chains. When brush-printing is applied, a shear stress is developed across the polymer solution. There are two boundaries: the polymer solution–substrate and the polymer solution–brush interfaces. The increased ordering of the polymer is likely caused by effective application of shear stress to the polymer chains across the entire depth of the polymer solution during the brushing process (23, 24). The variation in structural and electrical properties with the brush-printing speed supports the importance of the imposed shear stress.

Charge Transport—Morphology Correlations. Natural brush-printing was applied here as an effective tool to unravel the mechanism of charge transport in different families of semiconducting polymers. The experimental data presented here encompassing multiple polymers and deposition parameters directly address the interplay of shear–microstructure evolution–charge transport. The dependence of *DR* and charge transport anisotropy on brush-printing speed is shown in Fig. 4*C*. A minimal charge transport anisotropy of ~1.2 is

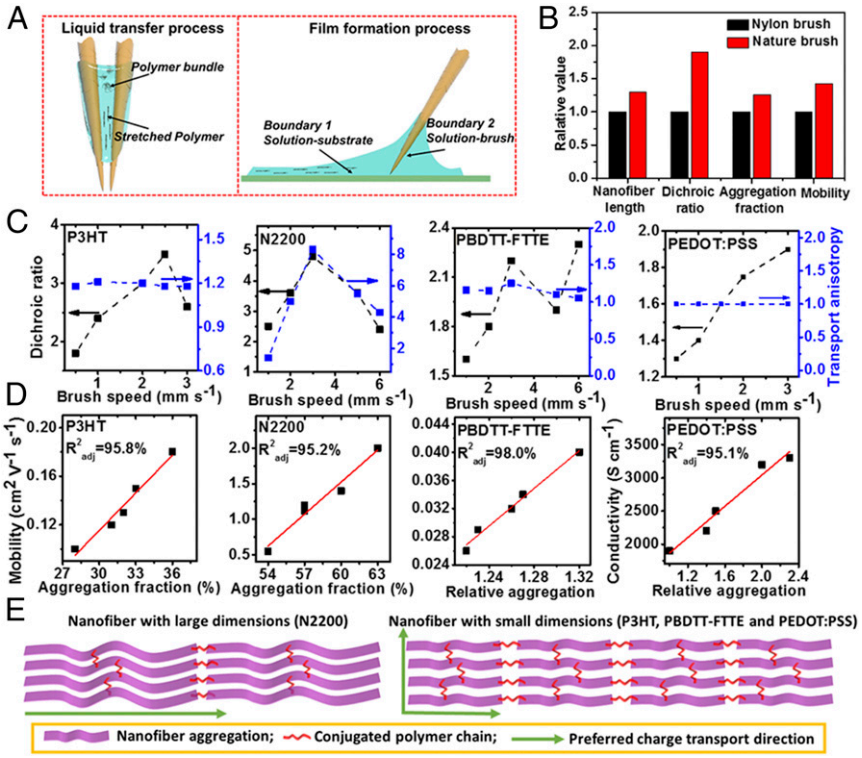

Fig. 4. Proposed mechanism for natural brush-printing and shear-induced charge transport. (*A*) Model for polymer conformational alteration, alignment, and aggregation/crystallization in liquid transfer and film formation process using brush-printing. (*B*) **N2200** films deposited by a Nylon brush and natural brush. (*C*) Dependence of *DR* and charge transport anisotropy on brush-printing speed. (*D*) Correlation coefficient of aggregation and charge transport. (*E*) Schematics for charge transport as a function of nanofiber dimension. (Note that the model for charge transport was simplified according to refs. 18, 19, and 28.)

observed for the **P3HT** and **PBDTT-FTTE** films, with negligible *DR* correlation. The **PEDOT:PSS** films exhibit no charge transport anisotropy coupled with backbone alignment. For **N2200**, there is an obvious charge transport anisotropy with a value up to eight at the optimal brush speed coupled with the largest *DR* of five. From the results summarized in Fig. 4*C*, we conclude that shear always enhances backbone alignment but does not necessarily induce charge transport anisotropy. For all polymers investigated here, the R^2_{adj} between aggregation and charge transport is as high as 95% (Fig. 4*D*), with SEs of 0.0107, 0.01678, 0.00952, and 132.2 for **P3HT**, **N2200**, **PBDTT-FTTE**, and **PEDOT:PSS**, respectively, which is low compared with their intrinsic mobility/conductivity. However, the correlation between backbone alignment and charge transport is 51.6% for **P3HT**, 61.9% for **N2200**, 31.8% for **PBDTT-FTTE**, and 19.2% for **PEDOT:PSS** (*SI Appendix*, Fig. S21). Thus, it can be concluded that the enhanced charge transport achieved via brush-printing can be attributed to the increased *AF* in each system examined. Fig. 4*E* shows the proposed mechanism of charge transport enhancement and anisotropy via brush-printing. During the brush-printing process, the extended polymer chains can be more easily packed to promote nanofibril aggregate growth, thus enhancing charge transport via densifying intermolecular packing. For **P3HT**, **PBDTT-FTTE**, and **PEDOT:PSS** nanofiber aggregation with small dimensions, charge transport depends on all aspects of film morphology, including polymer orientation, polymer–polymer relative orientation, polymer aggregate orientation, and aggregate domain connectivity. The minimal correlation of charge transport anisotropy and polymer backbone alignment likely reflects (*i*) small aggregation dimensions and (*ii*) contributions of amorphous portions and aggregation boundaries in the film (17).

In most semiconducting polymers, charge transport is primarily intramolecular in nature, with charge transport along the backbone as well as interchain hopping in the π–π stacking direction (53). **P3HT** nanofibers are reported to be interconnected by tie chains, which serve as bridges between well-aligned nanofibers to enable efficient charge transport (28). For **N2200**, larger-dimension nanofibril aggregation is imposed, and greater charge transport anisotropy reflects the tendency of **N2200** to form elongated chains, larger aggregate nanofibril dimensions, and pronounced face-on orientation (with respect to the substrate). Unlike **P3HT**, where the edge-on orientation (with respect to the substrate) favors in-plane charge transport, because of the highly face-on orientation of **N2200**, the contributions of intermolecular pathways are insignificant. When the **N2200** brush-printing direction is parallel to the source-drain electric field, electrons can be efficiently transported along the intramolecular direction parallel to the oriented nanofibril aggregates, and **N2200** chains at the aggregation boundaries can be elongated along the channel direction to serve as efficient intramolecular charge transport pathways. Thus, obvious charge transport anisotropy can be obtained for brush-sheared **N2200**. For brush-printing, charge transport mobility is promoted but will not necessarily induce charge transport anisotropy. With nanofiber aggregation, enhanced charge transport can be obtained in shear-printing. Thus, shear-induced aggregation is the key to enhanced charge transport. This work is likely to have applications in two emerging fields, organic thermoelectrics (54) and organic spintronics (55), where morphology effects on temperature–voltage and spin–charge conversion are little understood/investigated.

Conclusions

Natural brush-printing is applied here as an effective tool to realize direct aggregation control and to investigate the interplay between backbone alignment, aggregation, and charge transport anisotropy in π-semiconducting polymers. Through a systematic investigation involving multiple conjugated polymer classes differing in structure and transport properties, controllable nanofibril aggregate growth and backbone alignment are obtained, yielding remarkably increased mobilities of 0.21 $cm^2\ V^{-1}\ s^{-1}$ for p-type **P3HT**, 2.3 $cm^2\ V^{-1}\ s^{-1}$ for n-type **N2200**, and 0.044 $cm^2\ V^{-1}\ s^{-1}$ for p-type **PBDTT-FTTE** and a dc conductivity of 3,460 S cm^{-1} for **PEDOT:PSS**. For all polymers investigated here, the R^2_{adj} correlation between aggregation and charge transport is as high as 95%. Such systematic investigations lead to a better understanding of the interplay of shear-printing–microstructure evolution–charge transport in conjugated polymers. (*i*) Shear-induced polymer aggregation is key to enhancing charge transport. (*ii*) Shear can promote backbone alignment, thereby facilitating aggregation and enhancing charge transport but not necessarily charge transport anisotropy. The work provides additional insights into the charge transport mechanism for shear-printing and serves as a guide for the rational design of next generation high-performance organic electronics.

Methods

Details of device fabrication and thin-film characterization, GIWAXS line cuts, and correlation coefficient plots can be found in *SI Appendix*.

Using a brush made of natural sheep hair (Lanxuan Company), conjugated polymer solutions were painted onto the substrates. The brush was held rigid during the film fabrication process, with the printing speed controlled by a motor (Fig. 1*A*). For the **P3HT**, **N2200**, and **PBDTT-FTTE** films, top-gate/bottom-contact OFETs were used. For **PEDOT:PSS**, a four-probe geometry was used to measure sheet resistance, with film thickness quantified by profilometry.

ACKNOWLEDGMENTS. This research was supported, in part, by the Argonne–Northwestern Solar Energy Research Center, an Energy Frontier Research Center funded by US Department of Energy (DOE), Office of Science, Office of Basic Energy Sciences Award DE-SC0001059 and Air Force Office of Scientific Research Grant FA9550-15-1-0044. Use of the Advanced Photon Source, an Office of Science User Facility operated for the US DOE Office of Science by Argonne National Laboratory, was supported by US DOE Contract DE-AC02-06CH11357. S.F. acknowledges support from Swedish Governmental Agency for Innovation Systems Grant 2015-04859 and Swedish Research Council Grant 2016-03979. E.F.M. was supported by Qatar National Priorities Research Program Grant 7-286-1-046. F.S.M. was supported by US Department of Commerce, National Institute of Standards and Technology Award 70NANB14H012 as part of the Center for Hierarchical Materials Design. This work made use of The Electron Probe Instrumentation Center, Keck-II, and/or Scanned Probe Imaging and Development facilities of Northwestern University's Northwestern University Atomic and Nanoscale Characterization Experimental Center, which has received support from Soft and Hybrid Nanotechnology Experimental Resource Grant NSF ECCS-1542205, Materials Research Science and Engineering Center Program NSF DMR-1121262 at the Materials Research Center, the International Institute for Nanotechnology (IIN), the Keck Foundation, and the State of Illinois through the IIN.

1. Yan H, et al. (2009) A high-mobility electron-transporting polymer for printed transistors. *Nature* 457:679–686.
2. Worfolk BJ, et al. (2015) Ultrahigh electrical conductivity in solution-sheared polymeric transparent films. *Proc Natl Acad Sci USA* 112:14138–14143.
3. Diao Y, et al. (2015) Flow-enhanced solution printing of all-polymer solar cells. *Nat Commun* 6:7955.
4. Guo X, et al. (2013) Polymer solar cells with enhanced fill factors. *Nat Photonics* 7: 825–833.
5. Diao Y, et al. (2013) Solution coating of large-area organic semiconductor thin films with aligned single-crystalline domains. *Nat Mater* 12:665–671.
6. Sun K, et al. (2015) A molecular nematic liquid crystalline material for high-performance organic photovoltaics. *Nat Commun* 6:6013.
7. Rivnay J, et al. (2009) Large modulation of carrier transport by grain-boundary molecular packing and microstructure in organic thin films. *Nat Mater* 8:952–958.
8. Lee BH, et al. (2016) Flexible organic transistors with controlled nanomorphology. *Nano Lett* 16:314–319.
9. Bucella SG, et al. (2015) Macroscopic and high-throughput printing of aligned nanostructured polymer semiconductors for MHz large-area electronics. *Nat Commun* 6:8394.
10. Luo C, et al. (2014) General strategy for self-assembly of highly oriented nanocrystalline semiconducting polymers with high mobility. *Nano Lett* 14: 2764–2771.
11. Kim B-G, et al. (2013) A molecular design principle of lyotropic liquid-crystalline conjugated polymers with directed alignment capability for plastic electronics. *Nat Mater* 12:659–664.
12. Choi D, Chang M, Reichmanis E (2015) Controlled assembly of poly(3-hexylthiophene): Managing the disorder to order transition on the nano- through meso-scales. *Adv Funct Mater* 25:920–927.

13. Yuan Y, et al. (2014) Ultra-high mobility transparent organic thin film transistors grown by an off-centre spin-coating method. *Nat Commun* 5:3005.
14. Kim N-K, et al. (2015) High-performance organic field-effect transistors with directionally aligned conjugated polymer film deposited from pre-aggregated solution. *Chem Mater* 27:8345–8353.
15. Zhang X, et al. (2016) Alignment and patterning of ordered small-molecule organic semiconductor micro-/nanocrystals for device applications. *Adv Mater* 28:2475–2503.
16. Schott S, et al. (2015) Charge-transport anisotropy in a uniaxially aligned diketopyrrolopyrrole-based copolymer. *Adv Mater* 27:7356–7364.
17. Shaw L, et al. (2016) Direct uniaxial alignment of a donor–acceptor semiconducting polymer using single-step solution shearing. *ACS Appl Mater Interfaces* 8:9285–9296.
18. Wang S, et al. (2015) Experimental evidence that short-range intermolecular aggregation is sufficient for efficient charge transport in conjugated polymers. *Proc Natl Acad Sci USA* 112:10599–10604.
19. Wang G, et al. (2015) Microfluidic crystal engineering of π-conjugated polymers. *ACS Nano* 9:8220–8230.
20. Wang G, et al. (2015) Flow effects on the controlled growth of nanostructured networks at microcapillary walls for applications in continuous flow reactions. *ACS Appl Mater Interfaces* 7:21580–21588.
21. Kleinhenz N, et al. (2016) Ordering of poly(3-hexylthiophene) in solutions and films: Effects of fiber length and grain boundaries on anisotropy and mobility. *Chem Mater* 28:3905–3913.
22. Wang G, et al. (2016) Conjugated polymer alignment: Synergisms derived from microfluidic shear design and UV irradiation. *ACS Appl Mater Interfaces* 8:24761–24772.
23. Kim SS, Na SI, Jo J, Tae G, Kim DY (2007) Efficient polymer solar cells fabricated by simple brush painting. *Adv Mater* 19:4410–4415.
24. Kim S-S, Na S-I, Kang S-J, Kim D-Y (2010) Annealing-free fabrication of P3HT:PCBM solar cells via simple brush painting. *Sol Energy Mater Sol Cells* 94:171–175.
25. Zhang P, et al. (2016) Brush-controlled oriented growth of TCNQ microwire arrays for field-effect transistors. *J Mater Chem C Mater Opt Electron Devices* 4:433–439.
26. Wang Q, Su B, Liu H, Jiang L (2014) Chinese brushes: Controllable liquid transfer in ratchet conical hairs. *Adv Mater* 26:4889–4894.
27. Wang Q, Meng Q, Wang P, Liu H, Jiang L (2015) Bio-inspired direct patterning functional nanothin microlines: Controllable liquid transfer. *ACS Nano* 9:4362–4370.
28. Chu P-H, et al. (2016) Toward precision control of nanofiber orientation in conjugated polymer thin films: Impact on charge transport. *Chem Mater* 28:9099–9109.
29. Li Z, et al. (2016) High performance all-polymer solar cells by synergistic effects of fine-tuned crystallinity and solvent annealing. *J Am Chem Soc* 138:10935–10944.
30. Eastham ND, et al. (2017) Small molecule acceptor and polymer donor crystallinity and aggregation effects on microstructure templating: Understanding photovoltaic response in fullerene-free solar cells. *Chem Mater* 29:4432–4444.
31. Lu L, Yu L (2014) Understanding low bandgap polymer PTB7 and optimizing polymer solar cells based on it. *Adv Mater* 26:4413–4430.
32. Kim N, et al. (2014) Highly conductive PEDOT:PSS nanofibrils induced by solution-processed crystallization. *Adv Mater* 26:2268–2272.
33. Chu P-H, et al. (2016) Synergistic effect of regioregular and regiorandom poly(3-hexylthiophene) blends for high performance flexible organic field effect transistors. *Adv Electron Mater* 2:1500384.
34. Usov I, Mezzenga R (2015) FiberApp: An open-source software for tracking and analyzing polymers, filaments, biomacromolecules, and fibrous objects. *Macromolecules* 48:1269–1280.
35. Niles ET, et al. (2012) J-aggregate behavior in poly-3-hexylthiophene nanofibers. *J Phys Chem Lett* 3:259–263.
36. Spano FC (2009) Analysis of the UV/Vis and CD spectral line shapes of carotenoid assemblies: Spectral signatures of chiral H-aggregates. *J Am Chem Soc* 131:4267–4278.
37. Chang M, et al. (2015) Photoinduced anisotropic assembly of conjugated polymers in insulating polymer blends. *ACS Appl Mater Interfaces* 7:14095–14103.
38. Himmelberger S, Vandewal K, Fei Z, Heeney M, Salleo A (2014) Role of molecular weight distribution on charge transport in semiconducting polymers. *Macromolecules* 47:7151–7157.
39. Steyrleuthner R, et al. (2012) Aggregation in a high-mobility n-type low-bandgap copolymer with implications on semicrystalline morphology. *J Am Chem Soc* 134: 18303–18317.
40. Fauvell TJ, et al. (2016) Photophysical and morphological implications of single-strand conjugated polymer folding in solution. *Chem Mater* 28:2814–2822.
41. Wei Q, Mukaida M, Naitoh Y, Ishida T (2013) Morphological change and mobility enhancement in PEDOT:PSS by adding co-solvents. *Adv Mater* 25:2831–2836.
42. DeLongchamp DM, Kline RJ, Fischer DA, Richter LJ, Toney MF (2011) Molecular characterization of organic electronic films. *Adv Mater* 23:319–337.
43. Rivnay J, et al. (2010) Unconventional face-on texture and exceptional in-plane order of a high mobility n-type polymer. *Adv Mater* 22:4359–4363.
44. Qu G, Kwok JJ, Diao Y (2016) Flow-directed crystallization for printed electronics. *Acc Chem Res* 49:2756–2764.
45. Rivnay J, Mannsfeld SCB, Miller CE, Salleo A, Toney MF (2012) Quantitative determination of organic semiconductor microstructure from the molecular to device scale. *Chem Rev* 112:5488–5519.
46. Palumbiny CM, et al. (2015) The crystallization of PEDOT:PSS polymeric electrodes probed in situ during printing. *Adv Mater* 27:3391–3397.
47. Lamberti G (2014) Flow induced crystallisation of polymers. *Chem Soc Rev* 43: 2240–2252.
48. Lagasse RR, Maxwell B (1976) An experimental study of the kinetics of polymer crystallization during shear flow. *Polym Eng Sci* 16:189–199.
49. Mykhaylyk OO, et al. (2010) Control of structural morphology in shear-induced crystallization of polymers. *Macromolecules* 43:2389–2405.
50. Schroeder CM, Babcock HP, Shaqfeh ESG, Chu S (2003) Observation of polymer conformation hysteresis in extensional flow. *Science* 301:1515–1519.
51. Caruso MM, et al. (2009) Mechanically-induced chemical changes in polymeric materials. *Chem Rev* 109:5755–5798.
52. May PA, Moore JS (2013) Polymer mechanochemistry: Techniques to generate molecular force via elongational flows. *Chem Soc Rev* 42:7497–7506.
53. Noriega R, et al. (2013) A general relationship between disorder, aggregation and charge transport in conjugated polymers. *Nat Mater* 12:1038–1044.
54. Wang S, et al. (2016) Thermoelectric properties of solution-processed n-doped ladder-type conducting polymers. *Adv Mater* 28:10764–10771.
55. Ando K, Watanabe S, Mooser S, Saitoh E, Sirringhaus H (2013) Solution-processed organic spin-charge converter. *Nat Mater* 12:622–627.